

Project Number: PH-LRR-4510

Geometrical Optimization of Extraordinary Magnetoresistance

A MAJOR QUALIFYING PROJECT REPORT
SUBMITTED TO THE FACULTY OF
WORCESTER POLYTECHNIC INSTITUTE
IN PARTIAL FULFILLMENT OF THE REQUIREMENTS
FOR THE DEGREE OF BACHELOR OF SCIENCE
BY

Lisa M. Pugsley

Submitted: April 25, 2011

Approved:

L. Ramdas Ram-Mohan, Advisor

Abstract

The extraordinary magnetoresistance (EMR) in metal-semiconductor hybrid structures was first demonstrated using a van der Pauw configuration for a circular semiconductor wafer with a concentric metallic inclusion in it. This effect depends on the orbital motion of carriers in an external magnetic field, and the remarkably high magnetoresistance response observed suggests that the geometry of the metallic inclusion can be optimized to significantly enhance the EMR. Here the theory and simulations to achieve this goal are considered by comparing various 2D structures in an external magnetic field to evaluate the EMR in them.

Acknowledgements

I would like to thank Professor Ram-Mohan for all of his support and encouragement throughout the project. I would also like to thank Zehao Li, Cody Ahheng, and Andrei Ilyashenko for their input on the theory and programming considerations, as well as Paul Kassebaum for his assistance with the graphical aspect of the project.

<i>CONTENTS</i>	1
-----------------	---

Contents

List of Figures	2
1 Introduction	3
2 Theoretical Considerations	6
2.1 The Action Integral	6
2.2 The Finite Element Method with \mathcal{C}_1 -Continuous Elements . . .	9
2.3 Boundary Conditions for Hermite Elements	11
3 Results	16
3.1 A Rectangular Metallic Region Embedded in a Semiconductor	16
3.1.1 The Magnetoresistance	20
3.2 Multiple Metallic Regions Embedded in a Semiconductor Wafer	23
3.2.1 Comparison of Magnetoresistance	26
4 Conclusions	29
4.1 Future Prospects	29
References	32

List of Figures

1	A 2D Reference Finite Element for Hermite Interpolation . . .	15
2	A Semiconductor Wafer with a Rectangular Metallic Inclusion	17
3	Square Embedded Region 1 with Zero Magnetic Field	18
4	Square Embedded Region 1 with Applied Magnetic Field . . .	18
5	Magneto-resistance for Square 1	19
6	Square Embedded Region 2 with Zero Magnetic Field	21
7	Square Embedded Region 2 with Applied Magnetic Field . . .	21
8	Magneto-resistance for Square 2	22
9	A Schematic for a Thin Semiconductor Wafer with Several Metallic Bars	24
10	“Maze” Structure 1 with Zero Magnetic Field	25
11	“Maze” Structure 1 with Applied Magnetic Field	25
12	Square Structure 3 for Comparison with Maze, Zero Field . . .	27
13	Square Structure 3 for Comparison with Maze, with Applied Field	27
14	Comparison of Magneto-resistance for Square 3 and Maze Struc- ture	28
15	A Schematic Diagram for a 3D Semiconductor-Metal Hybrid Structure	31

1 Introduction

Magnetic materials and artificially layered metals exhibit giant magnetoresistance (GMR) and manganite perovskites show colossal magnetoresistance (CMR), their nomenclature suggesting unusually high magnetoresistance (MR) of the structures in externally applied magnetic fields. However, patterned nonmagnetic InSb shows a much larger geometrically enhanced MR even at room temperature and with no magnetic materials [1]. This effect is so large that it has been called extraordinary magnetoresistance (EMR) [2, 3]. This phenomenon is a member of a class of effects labeled by EXX (piezoconductance (EPC) [4, 5, 6, 7], optoconductance (EOC) [8, 9, 10], and electroconductance (EEC) [11] being the other effects) observed in metal-semiconductor hybrid structures that show remarkably high response of the structure to external perturbations. The magnetoresistance (MR) is defined as $MR = [R(H) - R(0)]/R(0)$, where $R(H)$ is the resistance at finite field H . Because they are nonmagnetic and work at room temperature, EMR devices can be used in applications where typical magnetic sensors are not suitable. Furthermore, their performance continues to be impressive down to the nanoscale. Unlike traditional magnetic recording sensor technologies, such as GMR and tunnel magnetoresistive (TMR) sensors, where device resistance is determined by spin dependent scattering, EMR magnetoresistance is modulated by utilizing the Lorentz force to steer an electron current away from the high conduction metallic regions. The carrier velocity has a non-zero Hall angle with respect to the electric field which continues to be directed normal to the essentially equipotential metal-semiconductor interface.

Experiments were initially performed on a composite van der Pauw disk of a semiconductor matrix with an embedded metallic circular inhomogeneity that was concentric with the semiconductor disk. A finite element approach to modeling was developed earlier [12], and the calculated MR based on a diffusive model for the current-electric field relation ($\mathbf{J} = \boldsymbol{\sigma} \cdot \mathbf{E}$), provides a striking agreement with experimental results for the MR for the circular geometry [12]. A similar enhancement has been reported [1] for a rectangular semiconductor wafer with a metallic shunt on one side. The rectangular geometry with four contacts can be shown to be derivable from the circular geometry by a conformal mapping [13], and the rectangular geometry is the desired form, from device fabrication considerations as for most semiconductor devices. So it is natural to consider variations of the rectangular embedding of metal in a semiconductor as the most convenient for experimental fabrication. An application of our original shunt geometry is to use the EMR device as a read-head for reading out data from magnetic storage hard-disks [3, 14, 15, 16]. The planar geometry of thin wafers results in a device that is sensitive to magnetic fields perpendicular to the plane of the wafer rather than the more typical in-plane field sensitivity demonstrated by GMR and TMR. This characteristic enables consideration of integrating EMR into unique planar recording head configurations. Commercial efforts in this direction are already under way. Further elaborations on the geometric enhancement of MR are discussed in Ref. [17].

In this project, the promise of very high MR in the metal-semiconductor structures is considered by designing new schemes that could substantially enhance the EMR effect, and by modeling realistic two-dimensional (2D)

structures that could be fabricated using Au and InSb. Here the theory for such analysis is developed, and it is demonstrated that geometrical enhancement of MR can be increased considerably with no more effort than used in making devices employed in earlier experiments with simple shunt devices. Estimates are provided for devices of mesoscopic and nanoscopic dimensions, keeping in mind the recent technological advances in material fabrication today. The theoretical development, presented in Section 2 discusses the use of high accuracy finite elements with \mathcal{C}_1 , or derivative continuity. The use of Hermite interpolation polynomials [18] for this purpose allows us to implement the derivative boundary conditions at interfaces very much more accurately than with Lagrange interpolation polynomials. All potential function and current boundary conditions can be explicitly implemented with Hermite interpolation polynomials, given their \mathcal{C}_1 degrees of freedom. Results of the analysis are given in Section 3 followed by concluding remarks in Section 4.

2 Theoretical Considerations

In the presence of a magnetic field, the magneto-conductivity is given in terms of $\vec{\beta} = \mu \vec{H}$ where μ is the carrier mobility and H is the magnetic field.

In 3D, we have

$$\boldsymbol{\sigma} = \frac{\sigma_0}{1 + \sum_i \beta_i^2} \begin{pmatrix} (1 + \beta_x^2) & (-\beta_z + \beta_y \beta_x) & (\beta_y + \beta_z \beta_x) \\ (\beta_z + \beta_y \beta_x) & (1 + \beta_y^2) & (-\beta_x + \beta_y \beta_z) \\ (-\beta_y + \beta_z \beta_x) & (\beta_x + \beta_y \beta_z) & (1 + \beta_z^2) \end{pmatrix} \quad (1)$$

which reduces in 2D, with $\vec{H} = \hat{z}H$ and $\beta_z = \mu H$, to

$$\boldsymbol{\sigma} = \frac{\sigma_0}{1 + \beta_z^2} \begin{pmatrix} 1 & -\beta_z \\ \beta_z & 1 \end{pmatrix} \quad (2)$$

with only the x, y -components for the conductivity tensor. Here the intrinsic conductivity σ_0 is the conductivity in the absence of a magnetic field.

2.1 The Action Integral

In Refs. [12, 15], we showed that a finite element approach [19, 18] to the calculation of the MR in simple 2D structures provides remarkable congruence with experimental results. Only linear interpolation polynomials were used in the calculations. Here we display the details of the theoretical development of the calculations for more complex geometries in 2D. We will also employ \mathcal{C}_1 -continuous functions which provide significant advantages in terms of accuracy, and also in terms of explicitly applying current continuity con-

ditions at internal metal-semiconductor interfaces and derivative boundary conditions along the periphery.

In the present case of steady-state conditions the equation of continuity leads to

$$\nabla \cdot \mathbf{J} = 0 = \nabla \cdot (\boldsymbol{\sigma} \mathbf{E}), \quad (3)$$

or equivalently,

$$-\nabla \cdot \boldsymbol{\sigma} \cdot \nabla \phi(\mathbf{r}) = 0, \quad (4)$$

where the electric field \mathbf{E} is expressed in terms of a scalar potential ϕ . The use of variational methods provides fast, stable convergence in the calculations and we cast the problem using the principle of stationary action. The action integral from which this equation is derivable for Dirichlet boundary conditions is

$$A_0 = \int_0^T dt \sum_{\alpha} \left[\int_{\Omega_{\alpha}} d\mathbf{r} \frac{1}{2} \left(\partial_i \phi(\mathbf{r}) \sigma_{ij}^{(\alpha)} \partial_j \phi(\mathbf{r}) \right) \right]. \quad (5)$$

The sum over α is to account for the actions in different regions Ω_{α} with their different conductivities. In the steady state under consideration here, the integration over time is trivial. Let us consider a typical 4-probe system for measuring the MR in the structure (see Fig. 2). The presence of current boundary conditions at two of the ports, corresponding to derivative boundary conditions, requires a modification of the above action in order to ensure that the equation of motion can be derived consistently. We suppose that the steady current comes in at port P_1 , say, and leaves the structure at port P_2 . The additional terms that are needed can be identified by analytically

attempting to obtain the equation of motion as follows. A variation of A_0 with respect to the potential function ϕ together with the usual integration by parts leads to

$$\delta_\phi(A_0/T) = 0 = \sum_\alpha \left[\int_{S_\alpha} d\mathbf{r} \delta\phi \left(-\nabla \cdot \boldsymbol{\sigma}^{(\alpha)} \cdot \nabla\phi(\mathbf{r}) \right) \right] + \sum_\beta \int_{\Gamma_\beta} d\ell \delta\phi \hat{n} \cdot \left(\boldsymbol{\sigma}^{(\beta)} \cdot \nabla\phi(\mathbf{r}) \right). \quad (6)$$

Here β corresponds to the various contours at the peripheries of the various regions and \hat{n} is the normal to the counter-clockwise boundary paths in 2D. It is clear that if we had Dirichlet boundary conditions specifying the potential everywhere along the external periphery, the second term in Eq. (6), which we refer to as the surface term in both 2D and 3D, would vanish since ϕ is then fixed on the boundary. We note that (i) the requirement of continuity of the current across the metal-semiconductor interface always ensures that the integrals along Γ_2 and Γ_3 cancel (see Fig. 2). We also note that (ii) The potential at, say, P_3 is set to zero to give a reference potential, hence the boundary integral across Δ_3 is zero ($\delta\phi$ is zero there since ϕ is set to zero there and is therefore fixed in value). (iii) Our boundary conditions are not of the Dirichlet type along the outer periphery at the current ports so that the portions of Γ_1 corresponding to $\Delta_{1,2}$ require special consideration. Using the relation $\mathbf{J} = -\boldsymbol{\sigma}\nabla\phi(\mathbf{r})$, we can identify the integrand of the surface term in square brackets in terms of the current there. Since no current comes in or escapes along Γ_1 except at the ports P_1 and P_2 , we can set the contour integral to zero everywhere along the periphery except over Δ_1 and Δ_2 . The

potential at port P_4 is determined by the solution on its being evaluated everywhere as discussed below. (*iv*) The two surface terms at $\Delta_{1,2}$ are such that $\delta\phi$ are arbitrary there, and $-\sigma\nabla\phi\cdot\hat{n}$ is nonzero. Since these two surface terms cannot be set to zero the equation of motion, Eq. (4), does not hold. This is remedied by adding two additional terms to the action that ensure that the surface terms are cancelled out [20, 12]. Writing the new action, we have

$$A/T = \sum_{\alpha} \int d\mathbf{r} \frac{1}{2} \left(\partial_i \phi(\mathbf{r}) \sigma_{ij}^{(\alpha)} \partial_j \phi(\mathbf{r}) \right) - \int_{\Delta_1} dl \phi(x, y) |_{\Delta_1} J_{in} + \int_{\Delta_2} dl \phi(x, y) |_{\Delta_2} J_{out} \quad (7)$$

with the current boundary conditions incorporated into the action. We note that while the current I_{in} must equal I_{out} , the width of the contacts $\Delta_{1,2}$ and the thickness of the semiconductor wafer determine the current densities $J_{1,2}$. The same considerations apply to a 3D geometry, and the extension of the above expressions to metallic inclusions in a semiconductor volume.

We now evaluate the action directly by discretization of the physical space using the finite element method (FEM), as discussed in the following.

2.2 The Finite Element Method with \mathcal{C}_1 -Continuous Elements

In the finite element method, the physical domain is discretized into elements. In each of the elements the variational principle holds. The potential function is represented as a polynomial multiplied by coefficients represent-

ing the value of the potential at special points in the element called nodes. On integrating out the spatial dependence, the action reduces to a bilinear expression in the as-yet unknown interpolation coefficients, which are known as the nodal variables. The principle of stationary action is invoked by varying A/T with respect to the nodal variables, which then leads to a system of simultaneous equations that represent the discretized equation of motion [18].

The spatial integrals are evaluated so that A/T is a function of just the nodal values. The stationarity of the action with respect to the variation of the nodal values leads to a set of simultaneous equations that are solved to obtain the potentials at the nodes. This allows us to obtain the potentials everywhere and also the currents in great detail, and we then determine the MR for a range of values of the magnetic field H .

Since the predominant practical choice of device geometry is rectangular, we consider finite elements of the same shape. In 2D, consider a standard square element with nodes at $\xi = \pm 1, \eta = \pm 1$. A given rectangular element can be linearly mapped into the standard element, so that the interpolation polynomials can be defined on the standard element for convenience. Each of the four nodes at the four corners of the element are associated with the values of the potential and its derivatives $\{\phi^{(in)}, \phi_{,\xi}^{(in)'} , \phi_{,\eta}^{(in)'} , \phi_{,\xi\eta}^{(in)''}\}$, where $in = 1, \dots, 4$, for the four nodes. Thus there are 4 degrees of freedom (DoF) at each of the four nodes of the element. This is shown in Fig. 1. The corresponding \mathcal{C}_1 -continuous (Hermite) interpolation polynomials are given in Ref.[18]. For Hermite interpolation polynomials $N_\nu(x, y)$, or shape functions as the interpolation polynomials are called in finite element analysis, we

represent the potential function over a given element as

$$\phi(x, y) = \sum_{\nu} \phi_{\nu} N_{\nu}(x, y), \quad (8)$$

with the sum running over the full set of 16 DoF for the element. The action is calculated over each element and the spatial variables are integrated out. The resulting expression is bilinear in the nodal variables and can be cast in a matrix form. The element matrices are then overlaid to account for the continuity of the solution over the individual materials of the composite, keeping account of the interface boundary conditions. In summary, the discretized action obtained from Eq.(7) can be written as

$$A/T \doteq \frac{1}{2} \phi_{\alpha} M_{\alpha\beta} \phi_{\beta} - \phi_{\alpha} [\delta_{\alpha\tau_1} R_{\tau_1}^{in}] J_{in} + \phi_{\alpha} [\delta_{\alpha\tau_2} R_{\tau_2}^{out}] J_{out} \quad (9)$$

where the surface integrals in Eq.(7) are designated by the nodal values multiplied by integration of shape functions only over the current ports in the last two terms.

2.3 Boundary Conditions for Hermite Elements

The boundary conditions for the potential and its derivatives are readily implemented within the finite element scheme.

- (a) The continuity of the potential across the metal-semiconductor interface can be enforced by setting the nodal values

$$\phi_{in}^I = \phi_{in}^{II}. \quad (10)$$

The continuity of the normal current across the interface requires

$$\hat{n}_i \sigma_{ij}^{(I)} \partial_j \phi^{(I)}(x, y) = \hat{n}_i \sigma_{ij}^{(II)} \partial_j \phi^{(II)}(x, y),$$

so that at each of the nodes common to the paths $\Gamma_{2,3}$ where, for example, $\hat{n}_\mu = \hat{y}$ we use the relation

$$\begin{pmatrix} 1 & 0 & 0 & 0 \\ 0 & 1 & 0 & 0 \\ 0 & \sigma_{yx}^{(I)} & \sigma_{yy}^{(I)} & 0 \\ 0 & 0 & 0 & 1 \end{pmatrix} \begin{pmatrix} \phi^{(I)} \\ \phi_x^{(I')} \\ \phi_y^{(I')} \\ \phi_{xy}^{(I'')} \end{pmatrix} = \begin{pmatrix} 1 & 0 & 0 & 0 \\ 0 & 1 & 0 & 0 \\ 0 & \sigma_{yx}^{(II)} & \sigma_{yy}^{(II)} & 0 \\ 0 & 0 & 0 & 1 \end{pmatrix} \begin{pmatrix} \phi^{(II)} \\ \phi_x^{(II')} \\ \phi_y^{(II')} \\ \phi_{xy}^{(II'')} \end{pmatrix}; \quad (11)$$

a similar relation holds for the current continuity of J_x across the interfaces with constant y . Thus the first-derivative degrees of freedom are reduced appropriately to enforce the current continuity. Note also that the tangential continuity of the electric field is assured by using the above transformation. (Recall that in the steady state, Faraday's law reduces to $\nabla \times \mathbf{E} = 0$, leading to the continuity of the tangential component of \mathbf{E} .) Also, we set the cross derivative of the potential to zero for the nodes at corners on the interface boundary.

- (b) No current enters or leaves the device on the outer boundary Γ_2 other than at the current ports. We therefore require that

$$J_n = \sigma_{nx} \frac{\partial \phi}{\partial x} + \sigma_{ny} \frac{\partial \phi}{\partial y} = 0, \quad (12)$$

except at the current ports. This again allows us to reduce the nodal

derivative degrees of freedom by one at every node on the external boundary. For $\hat{n} = \hat{x}$, we require $J_x = 0$; this implemented by setting the row corresponding to $\phi_{,x}^{(in)'} to zero, inserting σ_{xx} for the appropriate material at that node on that diagonal, and inserting σ_{xy} for the same material on the first supradiagonal on the same row. The variables $\phi^{(in)}$ and $\phi_{,xy}^{(in)''}$ at node in on the boundary are not preassigned any values since they have no conditions on them. A similar consideration holds for $J_y = 0$.$

- (c) At the voltage port P_3 , the potential at one of the nodes is set to zero to provide a voltage reference, while the normal current is eliminated as in the boundary condition (b) above. At the voltage port P_4 , the potential is not determined, but the normal current is again eliminated since no current leaves the system at P_4 .

As for the other degrees of freedom for these two ports, we treat them the same as the outer boundary since we do not want current going in or out.

The overlay of the calculations for the element matrices, consistent with the above element and interface boundary conditions, leads to the discretized action given by a global matrix M together with vectors representing the surface terms at the current ports. We have

$$A/T \doteq \frac{1}{2} \phi_\alpha M_{\alpha\beta} \phi_\beta - \phi_\alpha [\delta_{\alpha\tau_1} R_{\tau_1}^{in}] J_{in} + \phi_\alpha [\delta_{\alpha\tau_2} R_{\tau_2}^{out}] J_{out} \quad (13)$$

with the surface integral evaluated explicitly using the shape functions

mentioned earlier. The nodal values for the potential over the entire domain are labeled by ϕ_α , and their values at the current ports are limited to the nodes labeled by τ_1 and τ_2 that are located there. The principle of stationary action is implemented by varying the above discretized action with respect to ϕ_α and thereby obtaining the matrix equation that represents the original differential equation. We solve the matrix equation

$$M_{\alpha\beta}\phi_\beta = [\delta_{\alpha\tau_1} R_{\tau_1}^{in}] J_{in} - [\delta_{\alpha\tau_2} R_{\tau_2}^{out}] J_{out} \quad (14)$$

for the potential at the nodes over the entire domain.

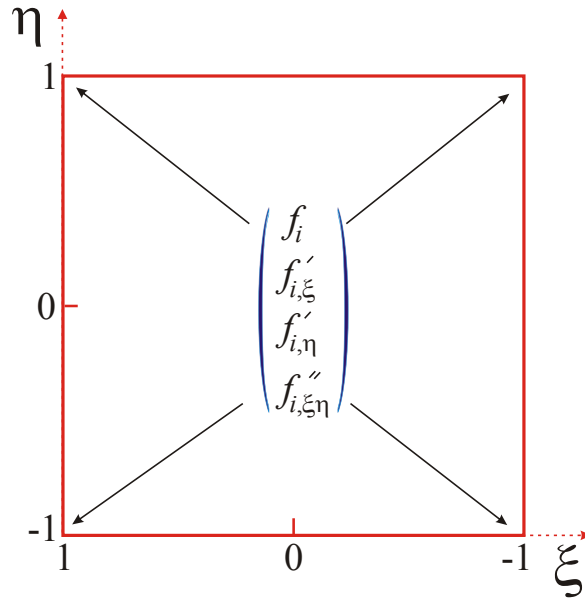


Figure 1: A 2D reference finite element with four degrees of freedom at nodes at the four corners corresponding to the value of the function, its first derivatives with respect to ξ, η and a second (cross) derivative. The polynomial interpolation within the element is performed using the values of the function and its derivatives at the nodes. See Ref. [18]. This scheme is extended to 3D for a cube element.

3 Results

3.1 A Rectangular Metallic Region Embedded in a Semiconductor

Fig. 2 shows the geometry in consideration, which is a rectangular region of Au embedded in InSb. Calculations were first done with the following port locations; for current in $(x, y) = (1 - 3, 0)$, and for current out $(x, y) = (7 - 9, 10)$. The results are show in Fig. 3 and Fig. 4. At a zero field, the current enters normal to the metal and goes through it, towards the current out port. In an applied magnetic field, however, the current is forced to take the longer path around the metal. These plots show side by side the magnitude and direction of the current flow, and the corresponding plot of the potential. In Fig. 3 and Fig. 4, the ratio of the amount of metal to the amount of semiconductor is one third. We can vary this ratio by changing the size of the interior metal region, which we are interested in because the increased size of the metal will result in a longer path for which the current is taking. Figure 5 shows a plot of the magnetoresistance versus the applied magnetic field, for various ratios of metal to semiconductor. It is obvious that as the ratio increases, the MR also increases substantially.

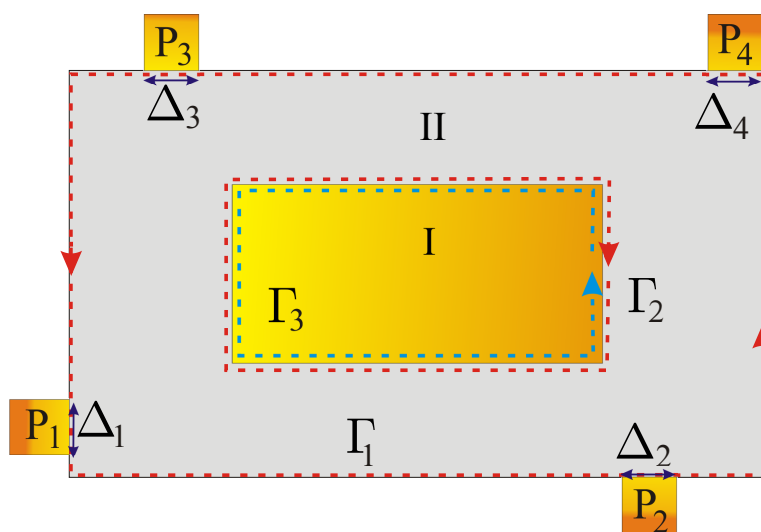


Figure 2: A semiconductor wafer with a rectangular metallic inclusion is shown. Contacts P_1, \dots, P_4 correspond to two voltage probes P_3 and P_4 , with current I coming in at say P_1 and leaving the structure at P_2 . The current density entering the device is taken to be $I/(\Delta_1 t)$ where t is the thickness of the wafer and Δ_1 is the width of the contact. The metal and semiconductor are labeled by roman numerals.

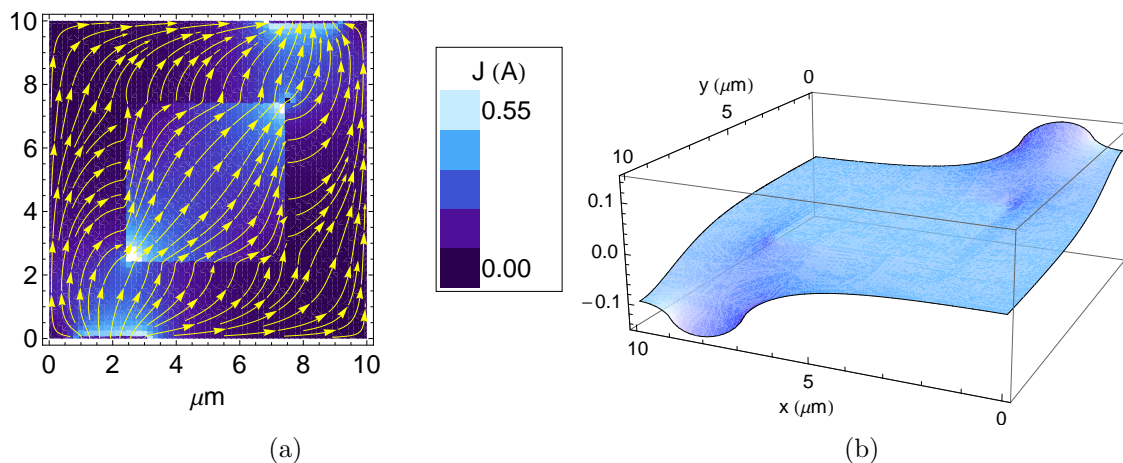


Figure 3: A square embedded region of Au with zero magnetic field. Plot (a) shows the current flow through the structure. The underlying gradient is representative of the magnitude of the current, where the arrows represent only direction. Plot (b) shows the potential, where the z -axis is in units of μV .

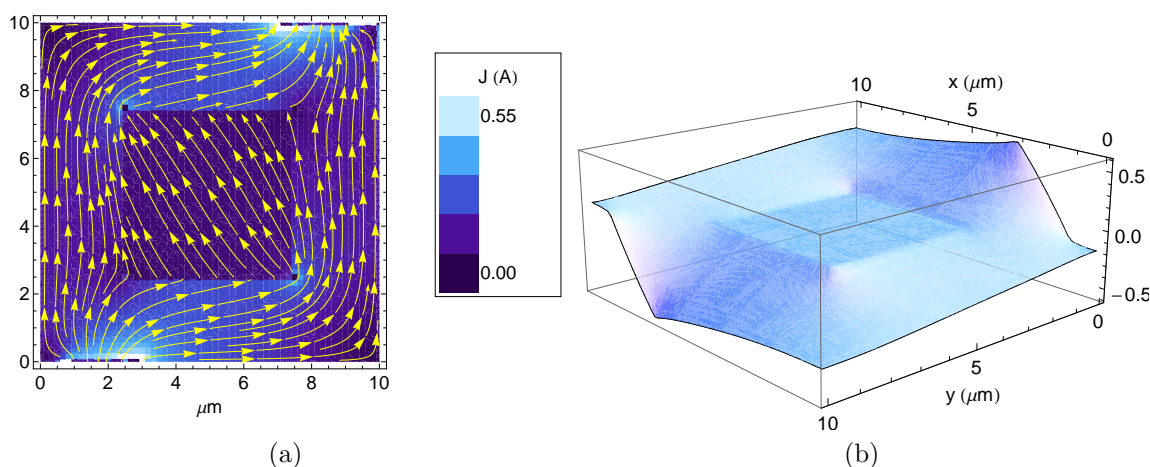


Figure 4: A square embedded region of Au with an applied magnetic field of -1 Tesla. Plot (a) shows the current flow through the structure. The underlying gradient is representative of the magnitude of the current, where the arrows represent only direction. Plot (b) shows the potential, where the z -axis is in units of μV .

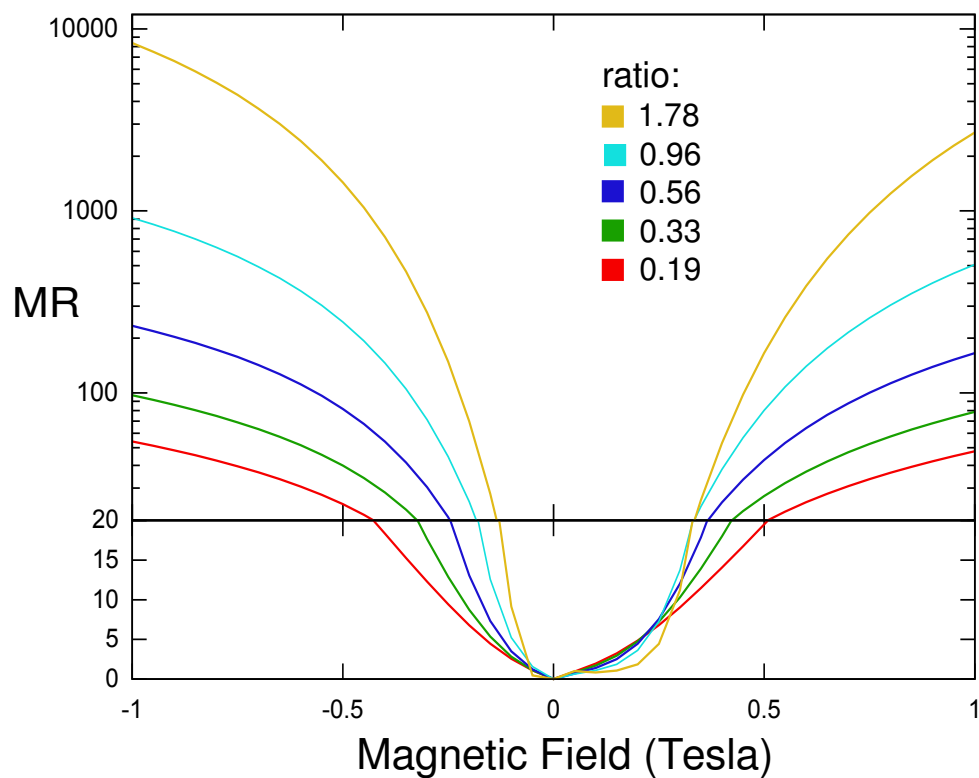


Figure 5: The magnetoresistance vs. applied magnetic field for the embedded square of Au discussed above. The absolute value of the MR is plotted.

3.1.1 The Magnetoresistance

For the previous scheme, we saw a very large MR response as our ratio of metal to semiconductor increased. In order to compare these results to previous calculations done on a circular geometry in Ref. [12] we must rearrange the current and potential ports to be analogous to those which were used for the circle. For this reason we choose new port locations which are: Port 1 (current in) at $(x, y) = (10, 4 - 6)$ and port 2 (current out) at $(x, y) = (4 - 6, 10)$. Port 3 is at the same y position as port 1 but at $x = 0$, and port 4 is opposite port 2. Results for the current and potential in this case are shown in Fig. 6 and Fig. 7. The plot of the magnetoresistance is shown in Fig. 8 below. Compared to Fig. 5, the maximum value is around the same. However, since the absolute value is plotted, one side of each plot is actually negative, and Fig. 5 is actually showing a higher change in MR than in this case.

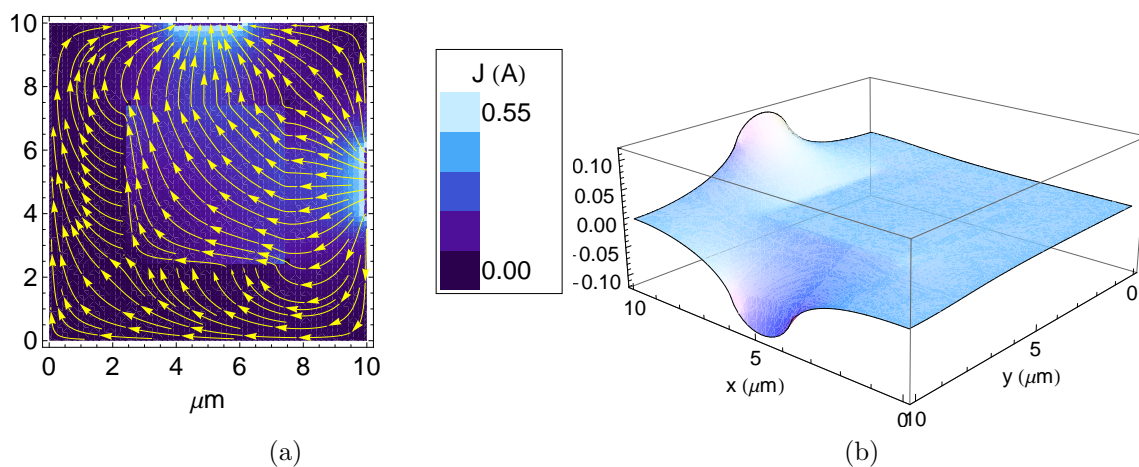


Figure 6: A square embedded region of Au with zero magnetic field. Plot (a) shows the current flow through the structure. The underlying gradient is representative of the magnitude of the current, where the arrows represent only direction. Plot (b) shows the potential, where the z-axis is in units of μV .

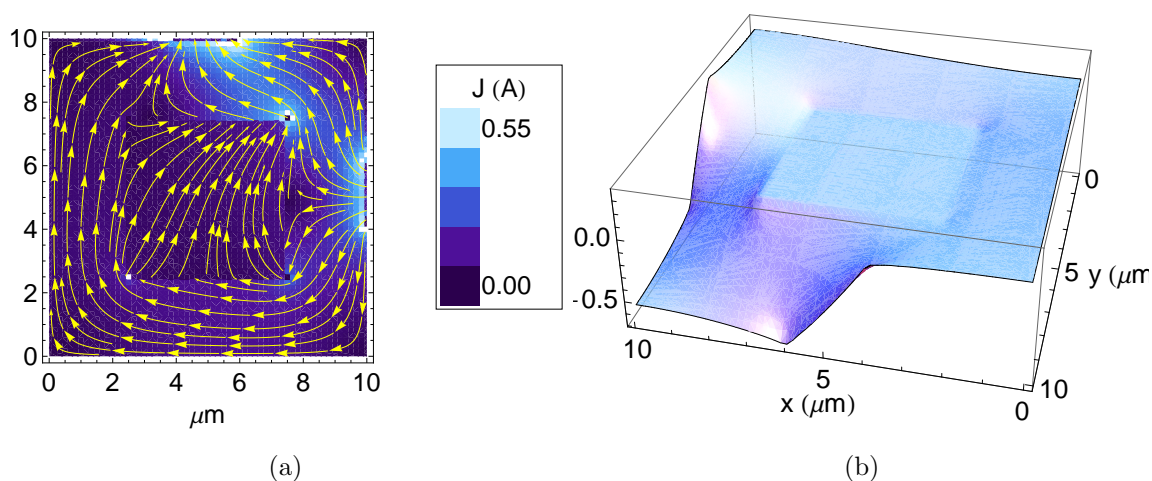


Figure 7: A square embedded region of Au with an applied magnetic field of -1 Tesla. Plot (a) shows the current flow through the structure. The underlying gradient is representative of the magnitude of the current, where the arrows represent only direction. Plot (b) shows the potential, where the z-axis is in units of μV .

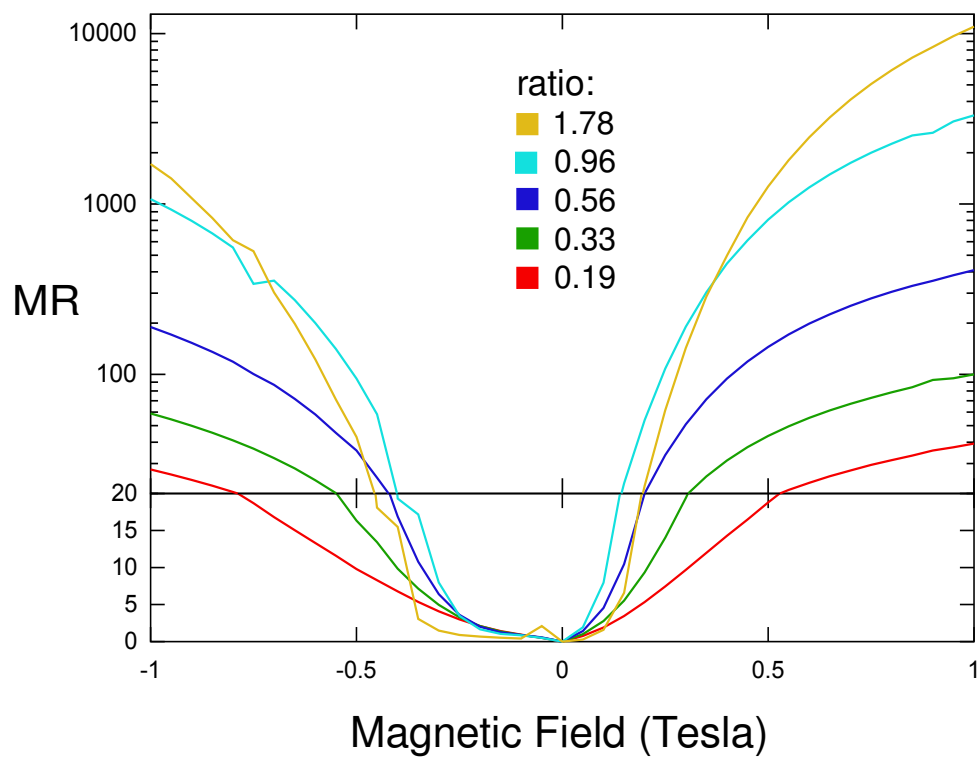


Figure 8: The magnetoresistance vs. applied magnetic field for the embedded square of Au discussed above. The absolute value of the MR is plotted.

3.2 Multiple Metallic Regions Embedded in a Semiconductor Wafer

Fig. 9 Shows the “maze” geometry which was chosen to see if the path of the current could be substantially increased. Figure 10 shows this structure for zero magnetic field and Figure 11 shows the same structure for an applied field of 1 Tesla. For the case of zero magnetic field, we see the same effect as before where the current goes through the metal towards the current out port. The current seems to mostly concentrate in the top and bottom most metal regions, because they are acting sort of as a parallel-plate capacitor. In an applied magnetic field, one would expect the current to take a winding path strictly around the metal regions. However, Figure 11 shows a different picture, where the current is still entering, or leaking through, at the corners of the metallic regions.

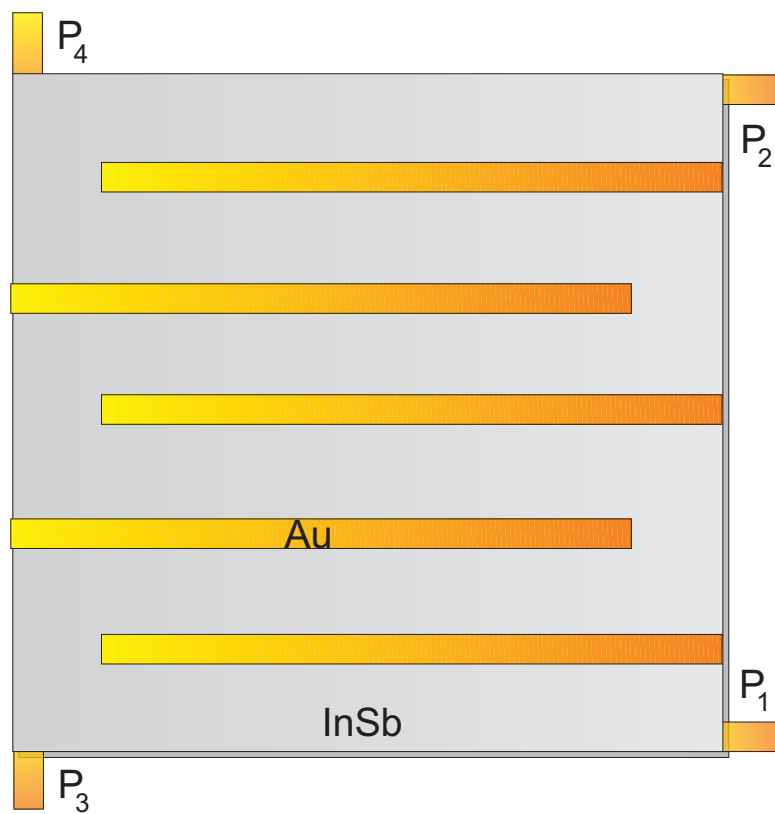


Figure 9: A schematic for a thin semiconductor wafer with several metallic bars, optimized to increase the carrier path in the semiconductor for finite applied magnetic fields. The increase in path translates into an increase in the MR. Contacts P_1, \dots, P_4 correspond to two voltage probes, with current I coming in at say P_1 and leaving the structure at P_2 .

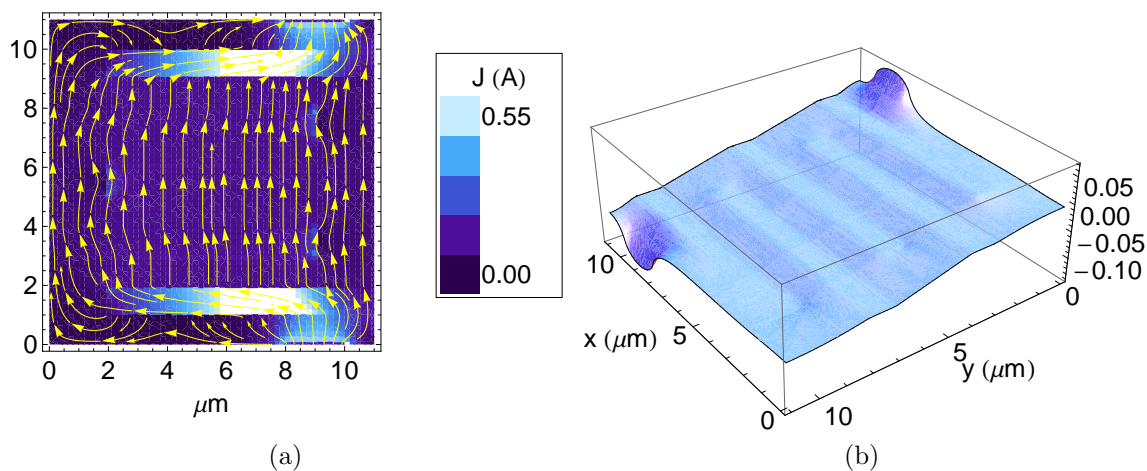


Figure 10: Shown are five embedded regions of Au with no applied magnetic field. Plot (a) shows the current flow through the structure. The underlying gradient is representative of the magnitude of the current, where the arrows represent only direction. Plot (b) shows the potential, where the z -axis is in units of μV .

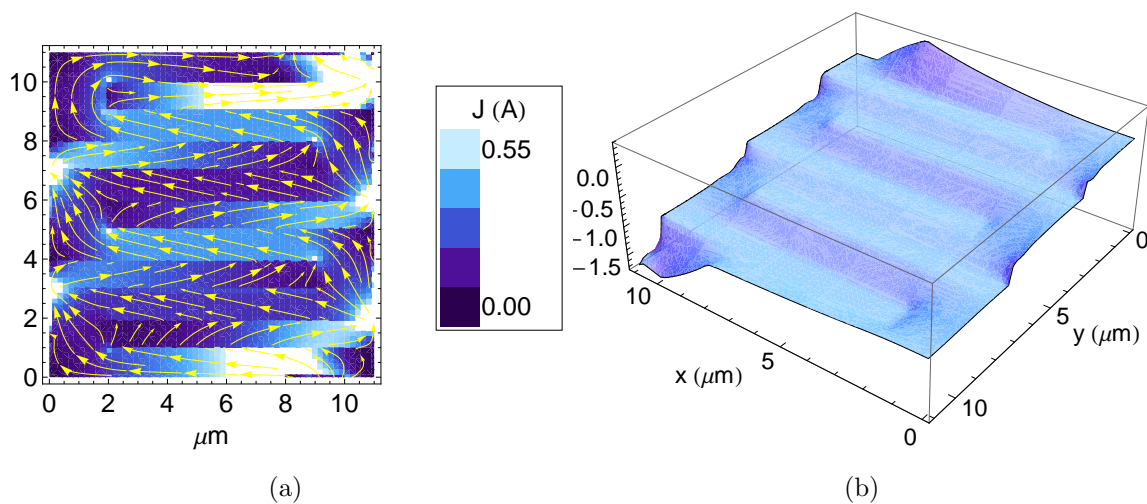


Figure 11: Shown are five regions of Au with an applied magnetic field of 1 Tesla. Plot (a) shows the current flow through the structure. The underlying gradient is representative of the magnitude of the current, where the arrows represent only direction. Plot (b) shows the potential, where the z -axis is in units of μV .

3.2.1 Comparison of Magnetoresistance

In order to see if the magnetoresistance is increased in the maze-like geometry, we must compare the MR to that of the case of the rectangular region, for which we already know shows the desired increase in EMR. However, we will once again rearrange the ports to be in the same position as in the maze geometry in Figure 10 and Figure 11. The result of this calculation is shown in Figure 12 and Figure 13. Figure 14 shows the comparison of the magnetoresistance between the two structures. It is apparent that at similar ratios of metal to semiconductor, the magnetoresistance for the maze structure is substantially less than that for the square with the same port locations. This means the path of the current in the maze structure must be shorter than in the square, since the current is leaking out through the metal. Also note that the port location in this case for the square results in a lower MR than in the previous two cases.

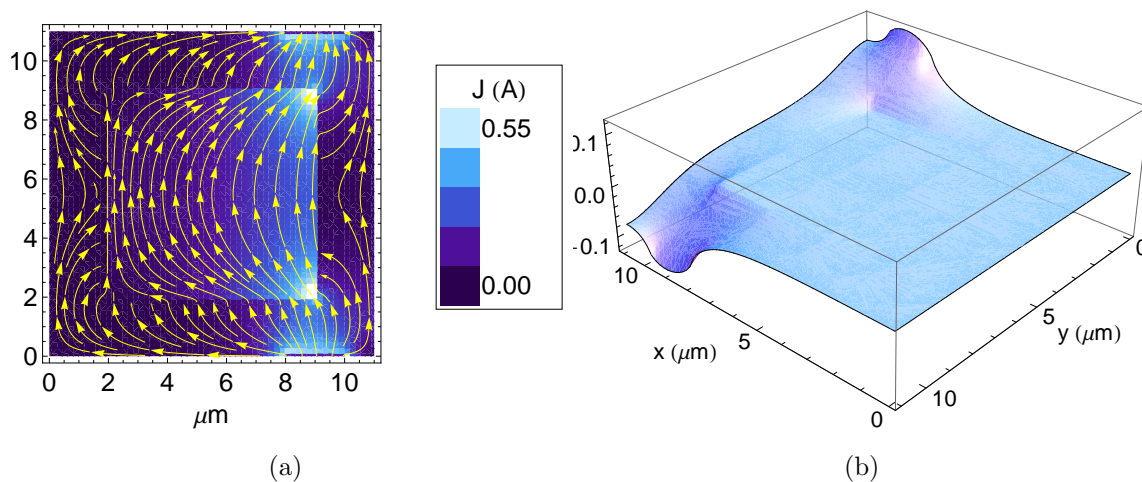


Figure 12: A square embedded region of Au is shown with zero magnetic field applied. Plot (a) shows the current flow through the structure. The underlying gradient is representative of the magnitude of the current, where the arrows represent only direction. Plot (b) shows the potential, where the z-axis is in units of μV .

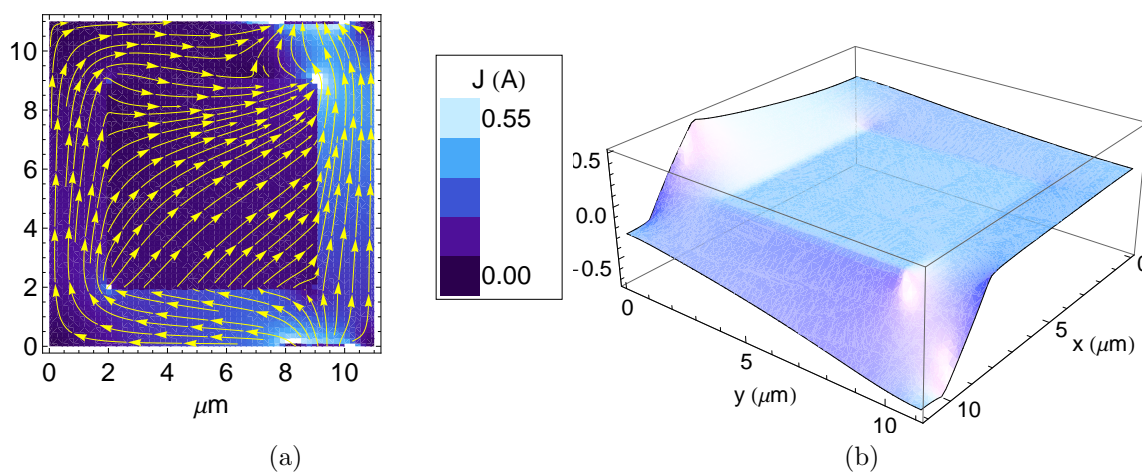


Figure 13: A square embedded region of Au is shown with an applied magnetic field of 1 Tesla. Plot (a) shows the current flow through the structure. The underlying gradient is representative of the magnitude of the current, where the arrows represent only direction. Plot (b) shows the potential, where the z-axis is in units of μV .

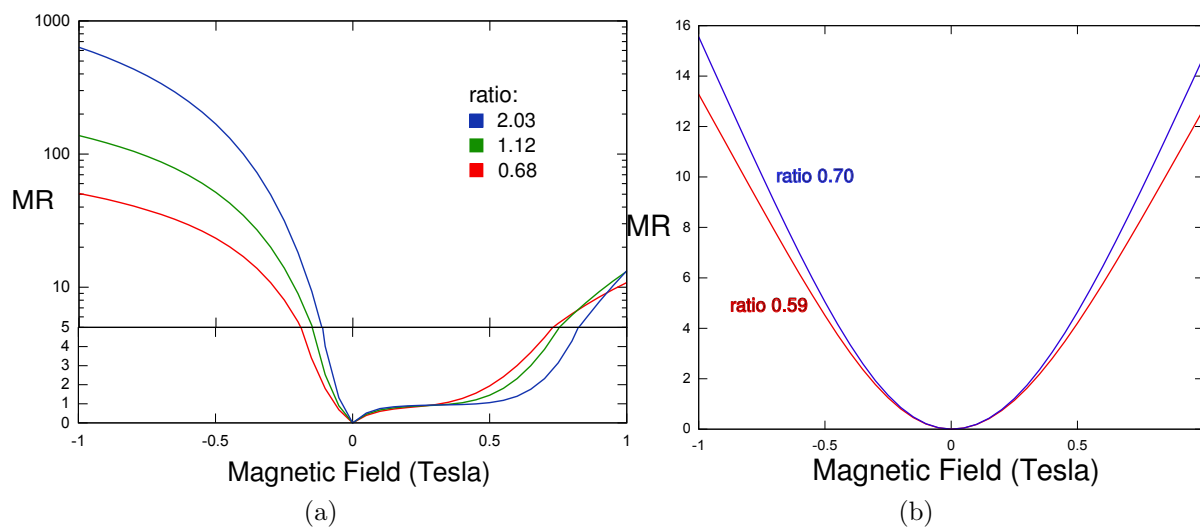


Figure 14: Figure (a) shows the MR vs. B for the square, in which the absolute value of the MR is plotted (the region from $x = [0:1]$ should be negative). Figure (b) is for the maze with ports in the same location. The MR in the maze is significantly lower than that in the square case.

4 Conclusions

It is clear that we can increase the magnetoresistance through changes in the geometry of a structure. The sensitivity of the device is based on intrinsic contributions from physical properties such as carrier mobility and energy band structure [17]. However there is also a geometric contribution to this, which can play an even more important role. The geometric contribution which can include the size and/or shape of the metallic regions and the device as a whole, the number of metallic regions, and even the orientation of the current and potential ports [17]. We can see this especially in the square geometry. Although the maze geometry did not show an increase in the MR, we can still explore a vast number of other scenarios in order to try to optimize the effect. It has been shown that the Finite Element Method produces highly accurate results, especially when using Hermite interpolation polynomials. FEM is advantageous because of the action integral formalism in which we can directly apply derivative boundary conditions for the current. It is also a very flexible method in which the possibilities for EMR calculations are endless.

4.1 Future Prospects

In the future, we can explore other 2D geometries in order to try to optimize the EMR. However, the theory and calculations presented here can also be extended to three dimensions. In this case we have even more degrees of freedom for Hermite interpolation (ϕ , ϕ'_x , ϕ'_y , ϕ'_z , ϕ'_{xy} , ϕ'_{yx} , ϕ'_{xz} , and ϕ'_{xyz}). We can consider a structure as shown in Figure 15, for which we can rearrange

the location of the ports anywhere we wish and also try new geometries for the metallic regions. For 3D it is possible to apply a magnetic field in any direction which also opens up many new possibilities.

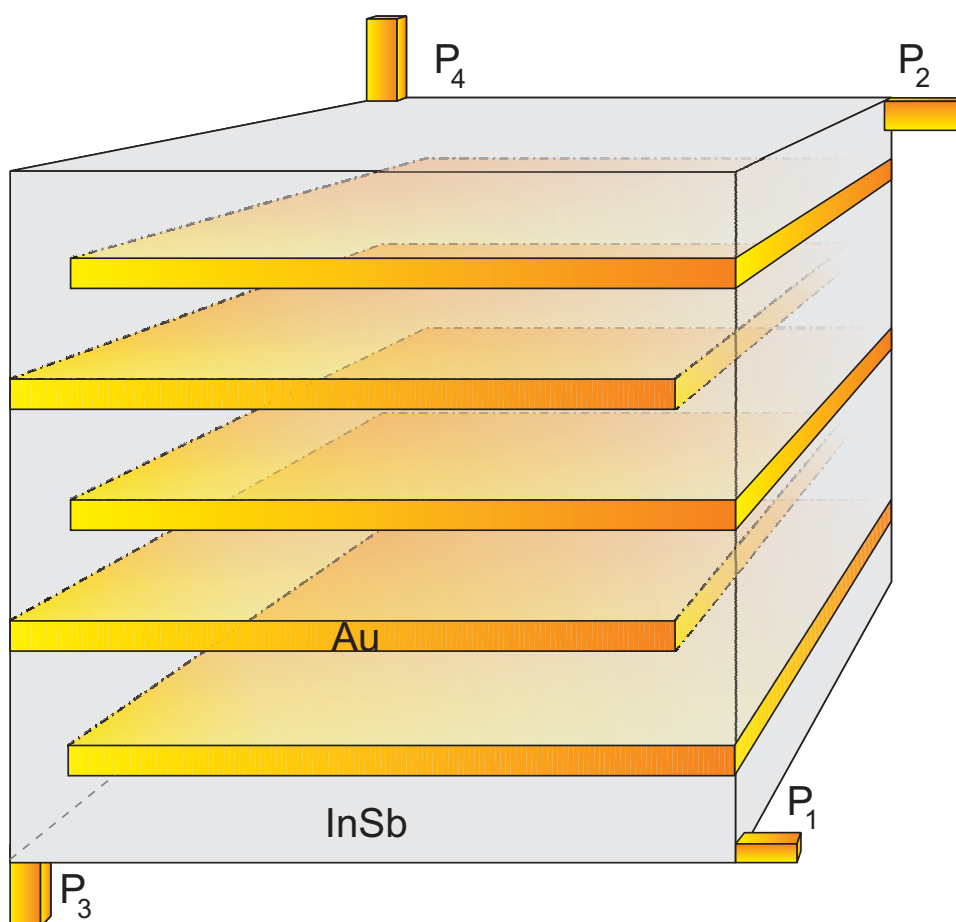


Figure 15: A schematic diagram for a 3D semiconductor-metal hybrid structure with metallic plates embedded in a semiconductor. In a magnetic field the plates do not act as shunts, diverting the carriers around them, leading to a much larger path within the semiconductor region. This enhances the MR. Contacts P_1, \dots, P_4 correspond to two voltage probes, with current I coming in at say P_1 and leaving the structure at P_2 .

References

- [1] S. A. Solin, Tineke Thio, D. R. Hines, and J. J. Hermans, *Science* **289**, 1530 (2000)
- [2] S. A. Solin, Tineke Thio, D. R. Hines, J. J. Heremans, and T. Zhou, *Proceedings of the 25th International Conference on the Physics of Semiconductors, Osaka, Japan*, edited by N. Miura (Springer, Berlin, 2001), pp. 1771-1774.
- [3] T. Zhou, D. R. Hines, and S. A. Solin, *Appl. Phys. Lett.* **78**, 667 (2001).
- [4] A. C. H. Rowe, K. Fasanella, T. Zhou, D. R. Hines, and S. A. Solin, *Rev. Sci. Instrum.* **73**, 4270 (2002).
- [5] A. C. H. Rowe, D. R. Hines, and S. A. Solin, *Appl. Phys. Lett.* **83**, 1160 (2003).
- [6] A. C. H. Rowe and S. A. Solin, *Phys. Rev. B* **71**, 235323 (2005).
- [7] A. C. H. Rowe, A. donoso-Barrera, Ch. Renner, S. Arscott, *Phys. Rev. Lett.* **100**, 145501 (2008).
- [8] K. Wieland, Y. Wang, L. R. Ram-Mohan, S. A. Solin, and A. M. Girgis, *Applied Physics Letters* **88**, 052105-052108 (2005).
- [9] K. Wieland, Y. Wang, S. A. Solin, A. M. Girgis, and L. R. Ram-Mohan, *Physical Review B* **73**, 155305-155312 (2006).

- [10] K. A. Wieland, Yun Wang, S. A. Solin, A. M. Girgis, and L. R. Ram Mohan, 28th International Conference on the Physics of Semiconductors, Vienna, Austria, AIP conf. Proc. 893, 1465 (2007).
- [11] Yun Wang, A. K. M. Newaz, Jian Wu, S. A. Solin, V. R. Kavasseri, N. Jin, I. S. Ahmed, and I. Adesida, Appl. Phys. Lett. 92, 262106 (2008).
- [12] J. Moussa, L. R. Ram-Mohan, J. Sullivan, T. Zhou, D. R. Hines, and S. A. Solin, Phys. Rev. B **64**, 184410 (2001).
- [13] R. S. Popovic, *Hall Effect Devices* (Adam Hilger, Bristol, 1991).
- [14] S. Solin, D. R. Hines, A. C. H. Rowe, J. S. Tsai, Y. A. Pashkin, S. J. Chung, N. Goel, and M. B. Santos, Appl. Phys. Lett., vol. 80, pp. 4012-4014 (2002).
- [15] J. Moussa, L. R. Ram-Mohan, A. C. H. Rowe, S. A. Solin, Journal of Applied Physics **94**, 1110 (2003).
- [16] S. A. Solin, Sci. Am. **291**, 70 (2004).
- [17] S. A. Solin and L. R. Ram-Mohan, Geometry-driven Magnetoresistance, in *Handbook of Magnetism and Advanced Magnetic Materials*, Edited by H. Kronmüller and S. Parkin, Volume 5: Spintronics and Magnetoelectronics (John Wiley & Sons, NY, 2007); pp1-21.
- [18] L. R. Ram-Mohan, *Finite Element and Boundary Element Applications to Quantum Mechanics* (Oxford University Press, Oxford, 2002).

- [19] O. C. Zienkiewicz and R. L. Taylor, *The Finite Element Method*, 4th ed. (McGraw-Hill, New York, 1994); T. J. R. Hughes, *The Finite Element Method* (Prentice-Hall, Englewood Cliffs, NJ, 1987).
- [20] R. Courant and D. Hilbert, *Methods of Mathematical Physics* (Interscience Publishers, New York, 1953).
- [21] M. Hoener, O. Kronenwerth, C. Heyn, D. Grundler and M. Holz, J. Appl. Phys. **99**, 036102 (2006).
- [22] M. Holz, O. Kronenwerth, and D. Grundler, Appl. Phys. Lett. **83**, 3344 (2003); Phys. Rev. B **67**, 195312 (2003); Appl. Phys. Lett. **86**, 072513 (2005).
- [23] T. H. Hewett and F. V. Kusmartsev, Phys. Rev. B **82**, 212404 (2010).